Polymer 49 (2008) 5158–5168

Contents lists available at ScienceDirect

Polymer

journal homepage: www.elsevier.com/locate/polymer

Examination of the effects of computationally determined network topology on an analytical constitutive model for bimodal elastomers

Paris R. von Lockette*

Mechanical Engineering, Rowan University, 201 Mulica Hill Road, Glassboro, NJ 08028, USA

ARTICLE INFO

Article history:
Received 3 July 2008
Received in revised form 21 August 2008
Accepted 22 August 2008
Available online 13 September 2008

Keywords:
Computational gelation
Polymer simulation
Bimodal PDMS

ABSTRACT

Bimodal elastomer networks, so called due to their nominal bimodal molecular weight distribution of starting oligomers, are of continued interest due to the enhanced strength and toughness seen in certain mixtures. Researchers have suggested that the enhanced properties stem from the particular micro-mechanics of the networks formed by these systems at these optimal compositions. This work extends an existing analytical constitutive model for bimodal elastomer networks by incorporating aspects of network topology, including network connectivity patterns and realistic chain length distributions, determined through computational simulations of the formation of the network structure. These factors are included as functions of bimodal composition and are shown to affect the predicted mechanical, optical, and orientation responses of the network. The extended model elucidates how the naturally occurring *doubled connection* topology creates a micro-mechanism that lowers overall chain orientation in the lower molecular weight component and recreates experimentally observed optical response phenomena. Specifically, the model predicts that the presence of the stiff, contractile, doubled connections forces the rest of the network to conform more to the macroscopic stretch ratio while reducing the measured average orientation of the lower molecular weight component in the system; the effect diminishes as the composition-dependent population of doubled connections in the system decreases.

1. Background

The fact that certain bimodal compositions of polydimethylsiloxane (PDMS) elastomer have shown anomalously high strength and toughness properties [1–3], and exhibited nonlinear stress–optic response in the small deformation range [4,5], led them to be a subject of continuing experimentation [6–9], modeling [10–12], and computational simulation [13–17]. These bimodal PDMS elastomers, so called because of their bimodal molecular weight distributions of starting oligomers, have shown up to five-fold increases in strength at certain mixture compositions. The history of the study of bimodal PDMS has been an effort to catalogue, to model and predict, and to explain the root causes of this behavior. A more detailed accounting of these past efforts can be found in Refs. [12,16,17].

The notion that the two components engage in differential load sharing within the elastomer network has emerged as a central tenet of this research. Key experiments and simulations suggesting that the more stiff short chains support more loading and that the more compliant long chains support less can be found in Refs. [9,13], as well as several others. Constitutive models which yield differential mechanical stretching in the two components of the material exist as well [10–12].

These efforts have prompted researchers to look more closely at the formation of the elastomer network microstructure of these materials [15–17] in an effort to develop improved models capable of explaining network response by incorporating effects of network topology on network behavior. This work focuses on extending an existing bimodal network constitutive theory [12] to include the computationally predicted evolution of network topology as it changes with changes in the constituents [17]. This extension provides a non-Gaussian, non-affine, phantom model which incorporates computationally predicted self-reinforcing topologies which form naturally during the computational crosslinking process. This new study highlights the direct effects of the computationally determined *doubled connection* topology, which was found to occur more predominantly in bimodal mixtures that showed increased strength and toughness [12], on the orientation and mechanical behavior of the network. Ref. [16] defines doubled connection found through computational simulations in the following manner:

> *Two tetra-functional agents in the gel may be connected by at most three molecular chains. A connection is defined as any chain or chains linking two separate reactive agents. The infrequent*

* Tel.: +1 856 256 5341; fax: +1 856 256 5241.
E-mail address: vonlockette@rowan.edu

0032-3861/$ – see front matter © 2008 Elsevier Ltd. All rights reserved.
doi:10.1016/j.polymer.2008.08.058

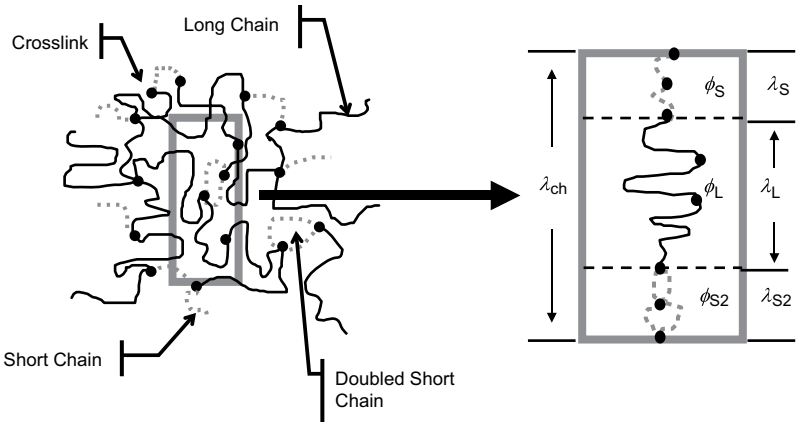

Fig. 1. Geometric contraction of a real bimodal network into a schematic of a representative series bimodal chain with short (S), long (L), and doubled short (S2) chain segments. The chain axis is considered a principal axes with respect to bulk deformation.

occurrence of tripled *connections is statistically insignificant. A* doubled connection *occurs when pairs of reactive agents are linked by two distinct molecular chains.*

The occurrence of the doubled connection topology has been reported in previous work and shown to correlate well with increased strength and toughness properties seen experimentally [16]. In addition, previous work that sought computationally to address the radial chain length distributions of bimodal networks in the annealed, undeformed state has found several results that reveal short-chain clustering in the simulated networks at certain mixture compositions [17]. These results mirrored short-chain clustering seen in previous light scattering experiments performed on bimodal PDMS [6,7].

For example, two-dimensional simulations clearly showed short-chain clustering occurring in bimodal networks having 85% short chains, but not in unimodal short chain systems given the same short chain molecular weights in both cases (see Ref. [17], Figs. 1 and 2). Similarly, the radial chain length distribution functions of undeformed, annealed, fully three-dimensional systems were shifted to lower values in bimodal systems as compared to unimodal networks having the same short chain molecular weights. Those shifted short chain distributions showed distinct upturns as the chain lengths approached zero indicating a sharp rise in the fraction of chains at very short ($r < (1/2)r_{rms}$) lengths. Results across a range of compositions similar to Table 2 also showed that as the fraction of short chains was increased (i.e. as it approached a unimodal short system) the effect was negated and clustering around the very short chain lengths ceased to occur [17].

Theoretical work outlined in Ref. [12] indicated that doubled short chains in the undeformed state existed at equilibrium lengths below that of singly-connected short chains, which would arguably increase the local clustering effect of the short chains. It is this very effect which is shown in this work to lead, theoretically, to a decrease in the combined measure of orientation of both the singly and the doubly connected short chains.

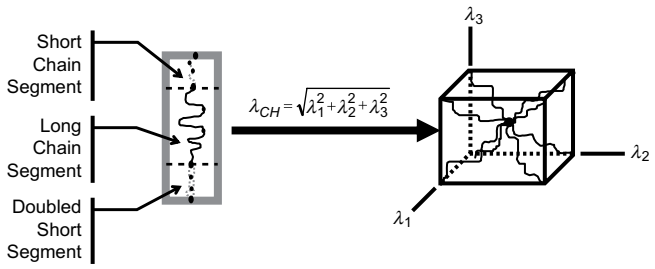

Fig. 2. Incorporation of the bimodal chain with S, L, and S2 segments in the eight-chain unit cube model for network averaging. Bimodal chain stretch ratio is a function of macroscopic principal stretch ratios, λ_1, λ_2, and λ_3. The unit cube is assumed to align with the principal axes of deformation.

The evolution of network structure is critical in our understanding of bimodal network behavior. The evolution of populations of specific self-reinforcing topologies has been cataloged previously and seems to play an important role in network reinforcement [16]. Therefore, it is informative to include the formation of these structures as a function of composition into a constitutive model. The addition to the bimodal constitutive model proposed here incorporates the results of network simulations performed on PDMS specimens given parameters to match those materials tested by the authors and those found in data in the literature by Mark [1,10]. Further, these simulated networks have been computationally annealed in order to generate more realistic *in situ* radial distribution functions of the short and long chains; this annealing step was shown to significantly shift the distributions by varying degrees based on the network's composition [17]. Evolution of network connectivity patterns is included by quantifying the occurrence of so-called *doubled connections* as a function of bimodal composition. The inclusion of these structure–property relationships aids in explaining mechanisms for the differential stretching and orientation seen experimentally in bimodal networks.

The following section will briefly highlight the existing constitutive framework discussed in Ref. [12], laying the foundation for this extension. The modeling presented in this work is an extension of a previously published bimodal chain theory; for more detailed argumentation for its basis and motivation please refer to Ref. [12]. The goal of this extension is to highlight the effects of incorporating the evolution of network structure (determined from computational simulation) into the original bimodal chain theory. Computational simulation techniques used in this work follow previously published methodologies and are discussed in Section 3.1. Incorporation of these topological effects causally reproduces behaviors indicative of those seen in actual experiments on PDMS, which allows the model to provide insight into bimodal network behavior.

2. Constitutive model for bimodal elastomers

2.1. Original bimodal chain model

The bimodal network theory begins with a geometric contraction of a real bimodal network into an idealized series arrangement

of long and short elastomeric molecules, or chains. The original model included a long chain and a short chain component comprised of long and short chains in series, respectively. A detailed discussion of arguments in favor of the series arrangement is given in Ref. [12]. In short, the series arrangement was initially chosen because it represented the preponderance of chain-to-chain connection modalities seen in computational simulations, e.g. singly-connected crosslinks. Parallel connections constituted less than 6% of the total number of connections in simulated networks [17]; most bimodal compositions had less than this maximum value of 6%. Even so, the current model overcomes this limitation by including parallel connections according to their populations in the simulations for a particular bimodal composition (see Fig. 1).

Each bimodal chain is assumed to behave according to the freely-jointed chain model which predicts differing force versus stretch ratio responses for the long and short chains. The freely-jointed chain model gives the force stretch ratio response of an elastomeric molecule represented as N randomly oriented, rigid steps of length d as

$$f = \frac{\kappa\Theta}{d}L^{-1}(\chi), \tag{1}$$

where κ is Boltzmann's constant, Θ is absolute temperature, d is the length of a Kuhn step, and χ is the fractional extension of the chain given by

$$\chi = \frac{r}{r_{\max}}, \tag{2}$$

where r is the current end-to-end vector length of the chain, and $r_{\max} = Nd$ is its maximum possible length. The Langevin function is defined as

$$L(\zeta) = \coth(\zeta) - \frac{1}{\zeta}, \tag{3}$$

such that its inverse is given by the familiar infinite series representation

$$\zeta = L^{-1}(\chi) = 3\chi + \frac{9}{5}\chi^3 + \frac{297}{175}\chi^5 + \cdots \tag{4}$$

The freely-jointed chain model assumes entropic concerns overshadow internal energy considerations which is consistent with prevailing theory on elastomers [18]. The force stretch ratio law is central to the derivation of the model because it dictates the force equilibrium constraints as will be shown in a later section.

2.2. Augmented bimodal chain model

The extended model now adds a doubled short chain component to the series arrangement of long and short chains owing to the computationally determined occurrence of statistically significant populations of this topology at mixtures that experimentally exhibit enhanced properties (see Fig. 1). In Fig. 1, a representative portion of a real network (shown boxed at left) is drawn schematically in a contraction of the structure (at right). The contraction, called a *bimodal chain*, is composed of a long chain component (L), a short chain component (S), and the new doubled short chain component (S2) in series. Essentially, the series arrangement in the bimodal chain reproduces *crosslink-to-crosslink* connectivity in its most probable and most direct mode of occurrence while the doubled connection topology, a parallel arrangement, incorporates what has surfaced as possibly important phenomena in bimodal networks. Network effects, i.e. interchain connectivity and the larger, more parallel-like structure generally associated with polymer networks, will be accounted for by incorporating the bimodal chain structure into a network averaging scheme.

The freely-jointed chain model's requirement of the determination of the current and maximum lengths of a constituent molecule during deformation and the chain arrangement lead to the natural development of geometric compatibility and force equilibrium constraints. With the inclusion of the doubled short chain component these constraints become nonlinear and differ greatly from the previously derived bimodal network theory.

2.3. Force equilibrium

Equilibrium between the L, S, and S2 components in a bimodal chain necessitates that

$$f_S = f_L = f_{S2}. \tag{5}$$

where f_i is the force in the i-th component. Assuming equivalent persistence lengths of chains in each segment and equivalent temperatures, the freely-jointed chain model of Eq. (1) in conjunction with equilibrium of the bimodal chain geometry yields

$$L^{-1}(\chi_S) = L^{-1}(\chi_L) = 2L^{-1}(\chi_{S2}), \tag{6}$$

where the factor of two on the last term stems from the existence of two chains per connection in the doubled connection segment. Adherence to Eq. (6) enforces equilibrium throughout the structure but more importantly it gives a direct apportioning of deformation between the S, L, and S2 components.

Equilibrium between S and L components, represented by the first two terms in Eq. (6) yields a simple relationship between fractional extensions,

$$\chi_S = \chi_L. \tag{7}$$

By first assuming that $r = \lambda r_o$ (where λ is the stretch ratio in the component) relates the current to original length of the chains in the segment, next that the original length is given by a scaled RMS length

$$r_o = \psi\sqrt{N}d \tag{8}$$

and finally that the maximum length is given by $r_{\max} = Nd$, the first equilibrium constraint, Eq. (7), reduces to

$$\frac{\psi_S\lambda_S}{\sqrt{N_S}} = \frac{\psi_L\lambda_L}{\sqrt{N_L}}. \tag{9}$$

The relationship in Eq. (9) provides a direct determination of the apportionment of stretch ratio between long chains and the short chains in the singly-connected segments of the bimodal chain. The RMS scaling, ψ, originates from the observed divergence of the simulated average initial lengths of chains in bimodal networks from the RMS assumption after computational annealing [17]. Deviation from the RMS assumption is incorporated into the model through ψ.

Force equilibrium between the S and L components, and the S2 component of the bimodal chain requires more complicated analysis. We first assume a relationship between the S and S2 component's fractional extensions,

$$\chi_{S2} = \beta\chi_S, \tag{10}$$

where β is a function of the S component's fractional extension that we write in polynomial form

$$\beta(\chi_S) = b_0 + b_1\chi_S + b_2\chi_S^2 + b_3\chi_S^3 + \cdots \tag{11}$$

such that from Eq. (6)

$$L^{-1}(\chi_S) = 2L^{-1}(\beta\chi_S). \tag{12}$$

Next we utilize a Padé approximation to the inverse Langevin to recast the constraint given by Eq. (12). The approximation is accurate within 1% over the range $\chi = [0,1]$; it is given by

$$L^{-1}(\chi) \approx \chi \frac{3-\chi^2}{1-\chi^2}. \tag{13}$$

Eq. (12) now becomes

$$\chi_S \frac{3-\chi_S^2}{1-\chi_S^2} = 2\left[(\beta\chi_S)\frac{3-(\beta\chi_S)^2}{1-(\beta\chi_S)^2}\right]. \tag{14}$$

Eq. (14) was solved numerically for β at 400 discrete values of χ_S over the range [0,1]. The numerical solution to Eq. (14) is a smooth, continuous function over [0,1] which is well approximated by the cubic polynomial given by $b_0 = 0.4985$, $b_1 = 0.0488$, $b_2 = -0.0423$, $b_3 = 0.5111$ (the regression coefficient associated with these coefficients is $R = 0.9997$). The maximum error in the approximation over the range $\chi_S = [0,0.97]$ is 0.52%; at $\chi_S = 0.99$ the error is 1.47%. The solution to Eq. (14) need only to be found once; it is valid for all fractional extensions in the relevant range.

The error in the solution to Eq. (14) is a direct assessment of the error in the force equilibrium constraint given in Eq. (5), or more apparently as it is cast in Eq. (12). The maximum error in the force balance on the range $\chi_S = [0,0.99]$ is less than 0.1%.

Combined with Eqs. (2), (10), and (11), the preceding analysis produces the desired S to S2 stretch ratio apportionment,

$$\chi_{S2} = \frac{\psi_{S2}\lambda_{S2}}{\sqrt{N_{S2}}} = \sum_{k=0}\beta_k\left[\frac{\psi_S\lambda_S}{\sqrt{N_S}}\right]^{k+1}. \tag{15}$$

Eqs. (9) and (15) give explicit relationships between stretch ratio in the S, L, and S2 components based on mechanical equilibrium directly. These stretch ratio relationships constitute a geometric compatibility constraint.

2.4. Geometric compatibility

Each component in the bimodal chain is composed of a number density, ϕ_i, of connections of type i = S, L, or S2. This number density is found from

$$\phi_i = n_i V_i, \tag{16}$$

where n_i is the number density of connections of type i in the network and V_i is the volume fraction of chains of type i in the network. In the representation, n_i's are not the standard unimodal-chain densities, but rather are defined as the densities of connections of a given type. This definition is used in determining the overall length and stretch ratio in the bimodal chain.

The stretch ratio of a bimodal chain can be determined from the sum of the lengths of the individual components according to

$$\lambda_{CH} = \frac{r_{CH}}{r_{CH\,o}} = \frac{l_S + l_L + l_{S2}}{l_{S\,o} + l_{L\,o} + l_{S2\,o}} = \frac{\phi_S r_S + \phi_L r_L + \phi_{S2} r_{S2}}{\phi_S r_{S\,o} + \phi_L r_{L\,o} + \phi_{S2} r_{S2\,o}}, \tag{17}$$

where r_{CH} and r_{CHo} are the current and original lengths of the entire bimodal chain, r_i and r_{io} are the current and original lengths of individual chain connections in segment type i, and $l_i = \phi_i r_i$ and $l_{io} = \phi_i r_{io}$ are the current and original lengths of an entire *i*-type segment, respectively. From Eq. (8) and the basic definition of stretch ratio, $r = \lambda r_o$, the stretch ratio in the bimodal chain is given by

$$\lambda_{CH} = \frac{\phi_S\psi_S\sqrt{N_S}d_S\lambda_S + \phi_L\psi_L\sqrt{N_L}d_L\lambda_L + \phi_{S2}\psi_{S2}\sqrt{N_{S2}}d_{S2}\lambda_{S2}}{\phi_S\psi_S\sqrt{N_S}d_S + \phi_L\psi_L\sqrt{N_L}d_L + \phi_{S2}\psi_{S2}\sqrt{N_{S2}}d_{S2}}. \tag{18}$$

Substitution of Eqs. (2), (8), (9) and (15) into Eq. (18) yields the stretch ratio in the bimodal chain as a function of its composition and the stretch ratio of the chains in its S component:

$$\lambda_{CH} = \left[\frac{1+(\phi_L N_L/\phi_S N_S)+(\phi_{S2}N_{S2}/\phi_S N_S)\sum_{i=0}\left[\beta_i\left(\psi_S\lambda_S/\sqrt{N_S}\right)^i\right]}{1+(\psi_L\phi_L/\psi_S\phi_S)\sqrt{(N_L/N_S)}+(\psi_{S2}\phi_{S2}/\psi_S\phi_S)\sqrt{(N_{S2}/N_S)}}\right]\lambda_S. \tag{19}$$

For any given amount of extension in the S component, Eq. (19) predicts the stretch ratio in the bimodal chain while Eqs. (9) and (15) will determine the stretch ratio in the L and S2 components, respectively.

It is important to point out that λ_{CH} is shown to relate nonlinearly to λ_S and that the nonlinearity increases as λ_S increases due to the series in the numerator of Eq. (19). This series represents the stiffness of the S2 component resisting the deformation of the bimodal chain. In fact, the results section will show that the stiffness of the S2 component will force higher levels of stretch ratio and orientation in the S and L components. As would be expected, as $\phi_{S2} \to 0$, the stretch ratio reduces to that given in Ref. [12] for a bimodal chain without an S2 segment. Also expected are the returns to unimodal cases if, with $\phi_{S2} = 0$, either $\phi_L \to 0$ or $\phi_S \to 0$, i.e. with fewer short chains the bimodal chain stretch ratio is characterized by the stretch ratio in the long chains and *vice versa*. The RMS scaling factor ψ, is also shown to play an important role in stretch ratio apportionment especially in light of the S2 contribution.

2.5. Network averaging

Network averaging is accomplished using the eight-chain contraction of a real network [19] (see Fig. 2). Each spar in the eight-chain model is composed of a bimodal chain that is in turn composed of S, L, and S2 segments subject to force and compatibility constraints. The spars radiate out from a central vertex to the corners of a unit cube oriented in the principal stretch ratio space. The model provides affine apportionment of stretch ratio from the macroscopic principal values to the bimodal chain, however, chain-level to segment-level stretch ratio apportionment is non-affine, i.e. the S, L, and S2 segments stretch ratio values relate non-affinely to the bimodal chain and thereby non-affinely to the macroscopic value. Principal stretch ratio values are related to the stretch ratio in a bimodal chain according to

$$\lambda_{CH} = \sqrt{\lambda_1^2 + \lambda_2^2 + \lambda_3^2} \tag{20}$$

where λ_i is the *i*-th principal stretch ratio. The eight-chain model was shown to be highly effective in capturing higher order terms of the orientation distribution function in Raman scattering experiments [20] and in capturing the stress–stretch ratio and stretch ratio–optic response in birefringence experiments in the two-component bimodal theory [12] as well as the large deformation stress [19] and stress–optic response in elastomers [21] warranting its further use here.

2.6. Stress–stretch ratio response

With the macroscopic-stretch ratio to chain segment–stretch ratio relationships known, the applied *stress* to macroscopic

stretch ratio response is found from the change in entropy of the bimodal chains in the unit cell as a function of macroscopic deformation. An expression for the entropy based on Langevin statistics [18],

$$s = c - \kappa N_k\left(\frac{r_k}{N_k d_k}B_k + \ln\frac{B_k}{\sinh B_k}\right); \quad B_k = L^{-1}\left(\frac{r_k}{r_k|_{\max}}\right), \quad (21)$$

gives the individual chain entropy in terms of the parameters associated with the chain connection type k, the stretch ratio as an argument to the inverse Langevin function, B, Boltzman's constant κ, and a reference value of entropy, c. The total entropy of the unit cell is then found from the sum of contribution from each type of chain connection in the network,

$$S = \phi_S s_S + \phi_L s_L + \phi_{S2} s_{S2}. \quad (22)$$

The total entropy expression in Eq. (22) leads to the principal stress difference via the well known relationship,

$$\sigma_i - \sigma_j = \lambda_i\frac{\partial W}{\partial \lambda_i} - \lambda_j\frac{\partial W}{\partial \lambda_j}, \quad (23)$$

where σ_i and λ_i are the principal stress and stretch ratio in the i-th direction. In Eq. (21), r values are taken from the scaled RMS assumption of Eq. (8). After applying Eqs. (16), (19) and (20), and the chain rule, the resulting expression for stress is given as

$$\sigma_i - \sigma_j = \frac{\kappa\theta}{3}G_1 G_2 L^{-1}\left[\frac{\Psi_S\lambda_S}{\sqrt{N_S}}\right]\left(\frac{\lambda_i^2 - \lambda_j^2}{\lambda_{CH}}\right), \quad (24)$$

where

$$G_1 = \left[\phi_L N_L + \phi_S N_S + 1/2\phi_{S2}N_{S2}\sum_{i=0}\left[(i+1)\beta_i\left(\frac{\psi_S\lambda_S}{\sqrt{N_S}}\right)^i\right]\right] \quad (25)$$

and

$$G_2 = \left[\frac{1+(\phi_L N_L/\phi_S N_S)+(\phi_{S2}N_{S2}/\phi_S N_S)\sum_{i=0}\left[(i+1)\beta_i\left(\psi_S\lambda_S/\sqrt{N_S}\right)^i\right]}{1+(\psi_L\phi_L/\psi_S\phi_S)\sqrt{N_L/N_S}+\psi_{S2}\phi_{S2}/\psi_S\phi_S\sqrt{N_{S2}/N_S}}\right] = \lambda_{CH}\lambda_S. \quad (26)$$

In Eq. (24) the principal stress-difference has the same form as the eight-chain model due to the similar unit cell geometry, however, the stress is shown to scale nonlinearly with the nonlinear stretch ratio apportioning of the short chains in Eqs. (25) and (26).

2.7. Stress–optic and orientation response

The birefringence of the unit cell network is derived from the polarizability, a direction dependent tensor quantity. Each spar in the unit cell, and consequently each chain type assumed to reside in each bimodal chain that comprises each spar, contribute to the overall polarizability of the unit cell and thereby to the birefringence. Detailed analysis of these relationships can be found in [18,20,22]. The resulting relationship for the birefringence is given as

$$\Delta\eta_{ij} = \left(\frac{2\pi}{9}\frac{(n_o^2+2)^2}{n_o}\right)[G_3 + G_4]\left(\frac{\lambda_i^2 - \lambda_j^2}{3\lambda_{CH}^2}\right) \quad (27)$$

where

$$G_3 = (\phi_S N_S\alpha_S + \phi_L N_L\alpha_L)(1 - 3Q_S) \quad (28)$$

and

$$G_4 = (\phi_{S2}N_{S2}\alpha_{S2})\left[1 - 6Q_S\sum_{k=0}\beta_k\left[\frac{\psi_S\lambda_S}{\sqrt{N_S}}\right]^k\right] \quad (29)$$

and

$$Q_S = \frac{3\left(\psi_S\lambda_S/\sqrt{N_S}\right)}{L^{-1}\left(\psi_S\lambda_S/\sqrt{N_S}\right)}. \quad (30)$$

In Eq. (27) the form of the eight-chain model's birefringence relationship is preserved, however, the nonlinear effects of network topology are apparent in Eq. (29) where the contribution of the S2 connections is scaled by a nonlinear dependence on the short chain stretch ratio. It will be shown later that the difference in microscopic stretch ratios between S and S2 components may account for experimentally measured differences in orientation between the short and long chains in bimodal systems.

2.8. Network topology and parameters

The bimodal network theory as described herein allows for the incorporation of microstructural changes in topology through six adjustable (best-fit) parameters and four fixed parameters found from simulations. The six adjustable parameters are three unimodal-chain number densities, $\overline{n}_S$, $\overline{n}_L$, and $\overline{n}_{S2}$ and three numbers of rigid Kuhn steps per chain, N_S , N_L , and N_{S2}. These control the initial modulus and the locking stretch ratio of unimodal samples of each type. Logical constraints, however, will eventually reduce the number of best-fit parameters to four.

The population of doubled short chain connections in the system, ξ, is the primary fixed parameter. This parameter measures the fraction of short chain connections that are doubled. The actual *connection* number densities of the S and S2 components in the network, n_S and n_{S2} , are two additional fixed parameters derived from ξ. The values of n_S and n_{S2} are found from the standard unimodal short chain density, $\overline{n}_S$, scaled by this computationally determined population of doubled short chain connections. The relationships are given by

$$n_{S2} = \frac{2\xi}{1+\xi}\overline{n}_S \quad (31)$$

$$n_S = \frac{1-\xi}{1+\xi}\overline{n}_S \quad (32)$$

The relationship $\overline{n}_S = n_{S2} + n_{S2}$ must hold, reflecting that the total number of short chains per unit volume will equal the sum of singly and doubly connected short chains per unit volume. For example, if 50% of the short chain connections are doubled, then $\zeta = 1/2$, $n_{S2} = 2/3$ and $n_S = 1/3$ showing that two-thirds of the short chains per unit volume are involved in doubled connections (values are for illustration only).

Since there are not a significant number of doubled long chain connections, $n_L = \overline{n}_L$ is taken as the unimodal long chain connection density. In addition, since the S and S2 components represent the same molecular species, it is assumed that $N_S = N_{S2}$. With these assumptions, the model is reduced to having only four adjustable parameters, $\overline{n}_S$, $\overline{n}_L$, N_L and N_S. A further strength of the model is that only two sets of data of arbitrary composition are needed to determine best-fit parameters for an entire mole fraction spectrum of bimodal materials of a given molecular weight combination [12].

The remaining three structural parameters are the RMS scaling factors, ψ_S, ψ_L, and ψ_{S2}. The RMS scalings are determined by

comparing the averages of the annealed radial distributions found in simulations to the theoretical RMS lengths for freely-jointed chains with the given number of Kuhn steps, N_i. Previous research has shown that computationally annealed simulated networks of freely-jointed chains have chain length distributions which differ not only from the RMS assumption, but also from their unannealed counterparts [17]. Consequently, incorporation of the annealed structure into the constitutive model is an important improvement of this method over previous works that analyzed the structure of mechanically unequilibrated networks. In addition, it has been shown that the mean value of the radial distribution changes with composition [17] increasing the importance of the evolution of topology with composition.

3. Simulations and topology

3.1. Simulation algorithm and systems studied

Simulations for this work were performed using a periodic crosslinking algorithm called NETSIM developed by the author [16] following the work of Eichenger [23,24]. In previous works the algorithm has been shown to agree with sol/gel fraction calculations and experimentation on PDMS networks in the literature, has uncovered a doubled connection topology in simulated networks, and has shown evidence of possible short chain agglomeration in simulations similar to what has been seen by experimenters using light scattering experiments [16]. The NETSIM algorithm uses a phantom, static nearest-neighbor crosslinking methodology on a nearest-neighbor periodic reaction volume seeded with tetra-functional crosslinking sites and di-functional end-linking polymer chains. The algorithm can accommodate arbitrary bimodal molecular weight distributions of molecules with known persistence lengths. An outline of the procedure is given below. For more details, please see Ref. [16].

The nearest neighbor search that numerically models the crosslinking process matches tetra-functional crosslinking agents to di-functional end-linking molecular chains. The unreacted chain ends in the simulation are each matched to the closest available crosslinking agent whose current functionality is ≥ 1. The process marches forward in order of proximity up to a fixed reaction radius (from the chain end) that sets the extent of the reaction. The closest pairs 'react' first.

The real crosslinking event adds several complexities including reaction probabilities that vary with extent of reaction, current functionality of the crosslinking agent, distance between prospective reactants and kinematics of the reactants. However, the simulation procedure has been used in several works most notably those of Eichenger [23,24], and shows good agreement with experimental gelation studies for many different constituent topology combinations in those and other works [16].

In these simulations, at certain mixture ratios of long and short chains the spacing of crosslinking agents and the length of the short polymer chains are such that two crosslinking agents may find themselves closest to opposite ends of the same short chain; this appears to happen in higher proportions at some mixture ratios (and thereby spacings) over other mixture ratios, hence we see more doubled connections forming more often at these mixtures.

In relation to the possibility of "doubled connections" in the actual crosslinking process, the argument is that the crosslinking agents are distributed randomly, but their spacing can be measured relative to the end-to-end length of the average (short) molecular chain. Since the spacing of the crosslinking agents is governed by the ratio of constituents, their molecular weights, and the stoichiometry of the reaction, one can vary the relative spacing of the crosslinking agents by varying the constituents and achieve an optimum, with respect to the end-to-end chain lengths, that produces a higher probability of forming doubled connections. The optimum will, necessarily, change with composition as well. The occurrence of doubled connection in simulations provides a useful metric of changes in network topology that agrees well with experimentally determined changes in network strength and toughness [16].

The original NETSIM algorithm has been automated to perform large scale mapping of the connectivity characteristics of simulated networks formed from a range of bimodal mixture compositions. For this work, the algorithm sampled the structures of bimodal networks having short chain molecular weight $M_S = 260$–1060 at increments of 200 with a fixed long chain molecular weight $M_L = 21{,}300$. For each molecular weight combination the mole fraction of short chains, m_S, was varied from 60% to 100% in increments of 2%. These systems were chosen because a good deal of literature exists on the behavior of these materials at similar compositions [1,3,4,5,12,16,17,23,24]. Finally, each mixture of each molecular weight combination was simulated 10 times to generate an average of the structural characteristics. The nearest-neighbor periodic simulation cell was seeded initially with 2000 linear, end-linking chains, 500 tetra-functional reactive agents for perfect stoichiometry, and given parameters to simulate the end-linking process of vinyl terminated PDMS. This simulation size results in a representative volume element for this periodic structure. This choice of parameters is detailed in Ref. [16]. The simulations were performed on a small cluster of sun workstations and servers comprised of one Sunblade 2000, two Sunblade 1000s, and seven Sunblade V100s.

3.2. Simulations results

3.2.1. Doubled connections

Fig. 3 shows a surface plot of the number of connections that are doubled versus the mole fraction of short chains for simulated bimodal networks having the short chain molecular weights and mole fractions of short chains shown. The average number of doubled connections ranges from 20.1 to 95.7 with the number of doubled connections generally increasing with molar short chain content. The increase in the number of doubled connections from lower to higher short chain contents might seemingly follow from the increase in populations of short chains in the system since there are increasing numbers of short chains present, however, two regions of the graph contradict this logic. Fig. 3 shows a decline in the number of doubled connections as the short chain content passes 90% across all compositions. In addition, the graph shows a sharp decline in doubled connections, from roughly 80 down to 45 for a constant 100% short chain composition (the far right of the graph) as molecular weight decreases. These trends go against perfunctory expectations that suggest increasing populations of short chains will monotonically increase the populations of doubled connections.

Fig. 4 depicts the percentage of short chain connections that are doubled versus the mole fraction of short chains for the same bimodal networks as in Fig. 3. Trends in these data also contradict an assumption of increased doubled connections due solely to increasing short chain content. The average percentage of connections that are doubled ranges from 2.1 to 5.2% showing a peak in the light colored regions between 90% and 95% by mole short chains. The fact that the maximum percentage of connections that are doubled occurs at an intermediate mixture suggests that the increase is not a sole function of the number of short chains present. As with the numbers of doubled connections, Fig. 4 shows a steep reduction in the percentage of doubled connections with decreasing molecular weight at near unimodal short chain compositions (far right, lower corner of graph).

In Figs. 3 and 4 it is interesting to note that the formation of doubled connections is not solely a function of short chain

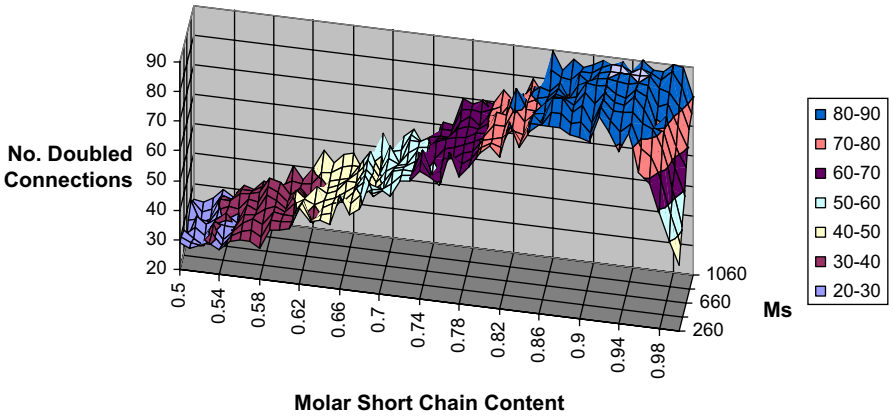

Fig. 3. Surface plot of the number of doubled connections versus molar short chain content for varying molecular weight of the short chains, M_S.

population since the percentages as well as the raw numbers of short chains that are doubled both increase with molar short chain content up until $m_S = 0.9$. The reversal of the trend, the decrease in the populations and percentages of doubled connections beyond $m_S = 0.9$, further suggests that other factors related to composition affect the topology of the networks formed. These results suggest that one can achieve an optimal spacing of crosslinks, with respect to the formation of doubled connections, for particular molecular weight combinations. At these optimal mixtures and resulting spacing the probability of forming a doubled connection is increased. In essence, when the average spacing of crosslinks nears the optimal value (near but not equal to the short chain length) the probability of forming a doubled connection increases. The probability decreases as the average distance between crosslinks moves away from the optimal spacing.

The surface plot data in Fig. 4 are used to construct an interpolation function relating the composition of the system, i.e. molecular weight of the short chains, M_S, and mole fraction of the short chains, m_S, to the percentage of doubled connections, ξ, predicted in simulations. This value of $\xi(M_S,m_S)$ was then used as a structural parameter in Eqs. (31) and (32) of the extended bimodal constitutive model. The form of the equation is given by

$$\xi = \sum_{i=0} c_i(M_S)^i + d_i(m_S)^i, \tag{33}$$

where c_i and d_i are constant coefficients found from polynomial least squares regression of the simulation data, and M_S and m_S are the molecular weight and mole fraction, respectively, of the short chain component of the bimodal system. The values of c and d are given in Table 1. Fig. 5 shows the graph of Eq. (33) and the values are given in Table 1. The figure shows that the interpolation does well in capturing the trend in peak values near $m_S = 0.90$ falling off as m_S is both increased and decreased, as seen in the simulations. The interpolation also somewhat captures the decrease in doubled connections as M_S decreases for the $m_S = 100\%$ cases.

3.2.2. Average end-to-end vector length

The averages of the annealed short chain radial distributions tabulated from simulations of various bimodal compositions are listed in Table 2. The specific bimodal compositions listed were chosen to match samples for which experimental stress–strain and stress–optic data are available in the literature. The table shows the average end-to-end vector length of short chain connections for several short chain compositions and molecular weight combinations. The RMS scaling factors for the i-type connections in each simulated network, ψ_i where i = short or long, are then found from

$$\psi_i = \frac{r_i}{r_{rms_i}}. \tag{34}$$

Fig. 6 shows the data of Table 2 as a graph of ψ_S versus mole fraction short chains for three molecular combinations. The data show interesting trends. For all three systems, the RMS scalings have initial values of roughly 0.75 for the unimodal short ($m_S = 100\%$) cases. In all three systems there is an abrupt increase in the magnitude of RMS scaling as the mole fraction of short chains is decreased; this increase in ψ, which occurs at different m_S values for each molecular weight combination, is followed by an abrupt decrease in ψ in two of the three cases. The shift in ψ values is either delayed or may not occur with an increase in long chain molecular weight as seen in system 880. This may follow a simple logic that as more long chains are introduced two things occur Eq. (1) the average spacing between crosslinks increases and Eq. (2) the networks are slow to move away from being short-chain dominated as more compliant material is added to the network.

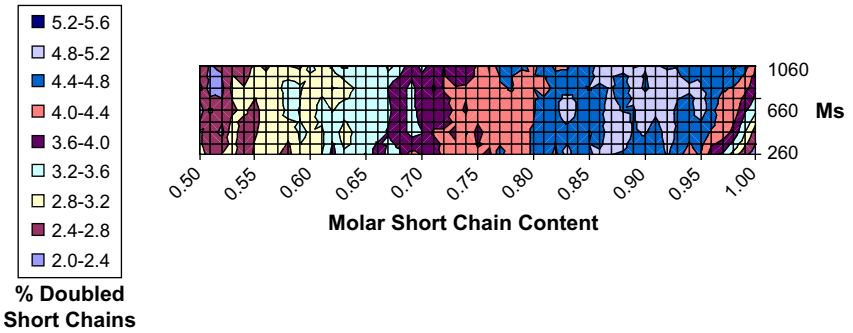

Fig. 4. Surface plot of the percentage of short chain connections that are doubled versus short molar chain content for varying molecular weights of the short chains, M_S.

Table 1
Values of regression coefficients predicting fraction of doubled connections in simulations

i	c	d
0	−3.717E+01	0.000
1	3.268E−03	226.884
2	−1.131E−05	−548.393
3	2.107E−08	789.394
4	−1.877E−11	−832.306
5	6.225E−15	630.602
6	0.000E+00	−226.156

The first point will directly increase the distance between short chains due to the lower chain density of higher molecular weight material. For a given volume, higher molecular weight linear end-linking materials require fewer crosslinking agents for stoichiometry. Therefore, the crosslink density will be lower resulting in increased spacing between crosslinks and consequently higher chain length distributions. This effect was seen and reported previously [16,17]. In Fig. 6 it is the cause of the increase in the short chain lengths in all three systems. This increase in spacing is matched in the long chains as well. Fig. 7 shows the average chain lengths of the long chains for the same three molecular weight combinations at the compositions as Fig. 6. Fig. 7 clearly shows the initial increase in spacing with the increase of long chain content as the amount of short chain material is reduced (and the amount of long chain material is increased).

The second point comes about due to the notion of the existence of mechanical equilibrium in the network. In general, higher molecular weight elastomers are more compliant than lower molecular weight elastomers. This is true of PDMS and has been evidenced experimentally in simple stress–strain experiments. It can also be seen theoretically from the freely-jointed chain model that as the number of statistical segments is reduced (analogously reducing the molecular weight) the stiffness of an individual elastomeric molecule, as characterized by the slope of its force vs. stretch ratio response, will stiffen.

In terms of a network, as more long chain material is introduced into the network, the network moves away from being a uniformly short chain dominated system to a heterogeneous one in which the existing short chain material forces the compliant long chain material to extend. To reach equilibrium between the short and long chains, the shorter chains must force this extension by contracting to shorter lengths. In a completely short chain dominated system this would not be possible, as evidenced by the nearly uniform scaling factors, ψ, for the unimodal short chain cases in Fig. 6, because all the chains have the same force versus stretch ratio response. Systems 460 and 660 show the expected decrease in short chain lengths with increasing long chain content beginning at 85% and 80% short chain compositions, respectively. The 660 system may be showing an extended region of elevated RMS scaling due to the increased crosslink spacing before the decrease resulting from the compliance of the existing long chains. A more complete study of this phenomenon is warranted.

The results of simulations yield both the percentage of connections that are doubled, ξ, and the RMS scaling factors, ψ_ι, for connections of types S, S2, and L. For this work, we assume $\psi_S = \psi_{S2}$ letting the effects of the doubled connections manifest themselves in the equilibrium constraints of Eqs. (10)–(15).

4. Modeling results

Figs. 8 and 9 show plots of stress versus stretch ratio for the bimodal chain model in uniaxial compression as evidence of its ability to characterize stress–stretch ratio data. The model without topology, Fig. 8, has been shown to agree well with stress–stretch ratio data for several molecular weight combinations having various mole fractions of short chains [12]. The model is fit to data on the 21,300-660 bimodal systems tested by Mark [1] yielding the model parameters in Table 3. The model is fit to data from the highest and lowest mole fraction cases only. The intermediate mole fraction response is predicted by the model's apportioning of stretch ratio.

Best-fit results of the extended bimodal theory which includes changing topology are given in Fig. 9. Computer simulations of the bimodal network predict a change in the RMS scaling, ψ, of the equilibrated (annealed), undeformed network (see Figs. 6 and 7) that necessitates recalculation of adjustable parameters n_S, n_L, N_S, N_L; the fixed parameters ψ_S and ψ_L, are taken from simulation results in entries of columns 4–6 Table 2 while ξ is found from simulation results characterized by Table 1 in conjunction with Eq. (33). The resulting fixed parameters for the extended bimodal theory are given in Table 4. Again, the fixed parameters are fit to the highest and lowest mole fraction cases, only; intermediate cases are fully predicted by the model.

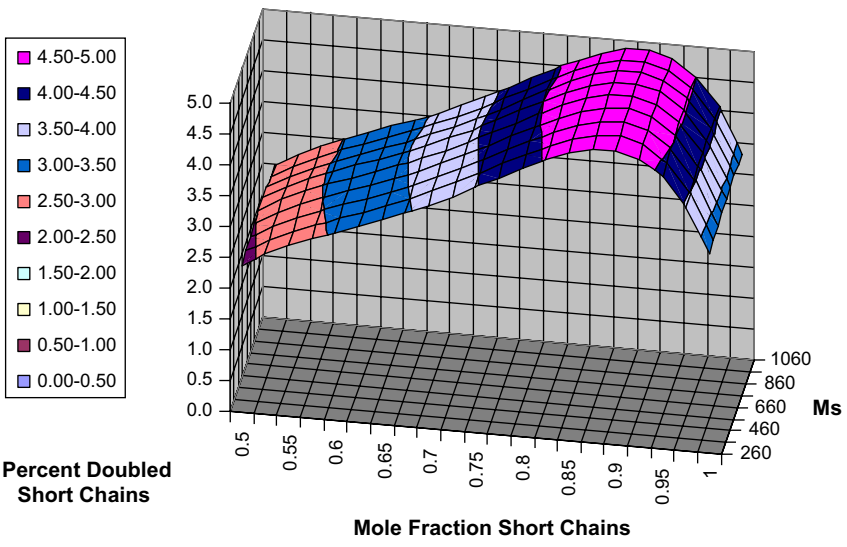

Fig. 5. Surface plot of the interpolated percentage of short chain connections that are doubled versus molar short chain content for varying molecular weight of the short chains, M_S. Interpolation coefficients taken from Table 1 are used in Eq. (33).

Table 2
Average annealed short chain lengths by short chain molecular weight and composition [17]; $M_L = 21{,}300$ for each case

Average of radial distribution of chain Lengths (Å)								
m_S	$M_S = 460$		m_S	$M_S = 660$		m_S	$M_S = 880$	
	Short	Long		Short	Long		Short	Long
0.60	6.39	94.45	0.60	7.68	95.20	0.60	18.91	103.07
0.85	9.73	108.09	0.80	11.07	109.74	0.80	18.82	101.68
0.91	13.70	103.99	0.85	18.15	105.58	0.85	14.19	106.24
0.92	14.38	100.74	.908	13.83	104.36	0.91	14.62	105.80
0.95	12.54	104.19	.942	13.53	101.63	0.93	15.01	105.65
0.97	12.41	99.65	.951	13.99	101.64	0.95	15.10	102.96
.995	10.98	98.71	0.97	13.88	101.09	0.97	14.95	100.49
1.00	11.09	NA	.985	13.47	102.25	0.98	14.54	102.98
			.994	13.62	103.14	0.99	14.92	101.78
			1.00	13.01	NA	1.00	14.49	NA

The compositions listed are chosen to correspond to data tested by Mark [1].

Figs. 8 and 9 are representative of similar good results on the complete mole fraction spectrums of bimodal PDMS systems having $M_S = 460$ and $M_S = 880$ both with $M_L = 21{,}300$ in uniaxial tension with topology included (not shown). The model with topology shows stress–stretch ratio results nearly indistinguishable from the model without topology for best-fit parameters matched to data except for a stiffening of the intermediate mole fractions' response. The stiffening of intermediate mixtures is indicative of load sharing that is better illustrated by observing stress–optic results.

The ultimate goal of this work is to model the load sharing behavior between the S, S2, and L components of the network, specifically how this load sharing may change with m_S and molecular weight distributions of the constituents. Herein, differential load sharing in bimodal networks is quantified by the difference in stretching and orientation of the components of the network; these phenomena can be measured by optical or spectral techniques. Previous analytical works have focused on predictions

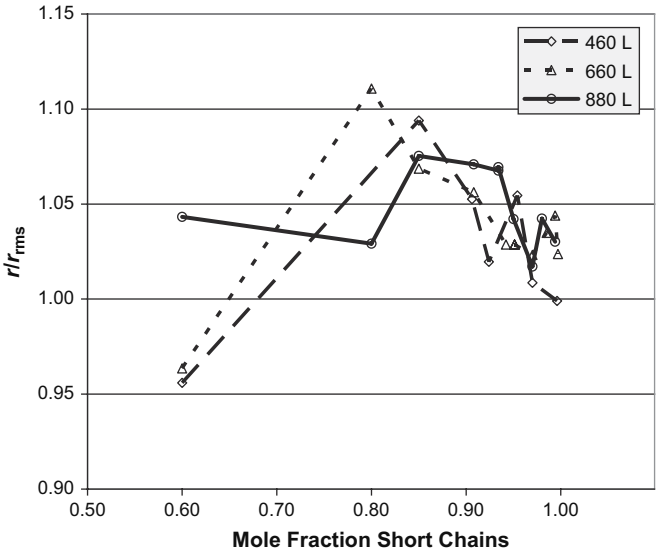

Fig. 7. Long chain connection RMS scaling factor, $\psi = r/r_{rms}$, for bimodal systems having short chain molecular weights of 460 (◇), 660 (△), and 880 (○) at the indicated molar short chain composition. Lines drawn for clarity.

of differential stretching as defined by $\lambda_S \neq \lambda_L$ [10,11] while experimental efforts focus on more readily measurable quantities such as the Herman's orientation function [8,9]. Herman's orientation function, e.g. the first moment of the orientation distribution function, is related to birefringence by

$$\frac{\Delta\eta}{\Delta\eta_{max}} = \frac{3\langle\cos^2\overline{\phi}\rangle - 1}{2}, \tag{35}$$

where the denominator on the left hand side of the equation is the calculated birefringence at a fractional extension of unity and $\overline{\phi}$ is

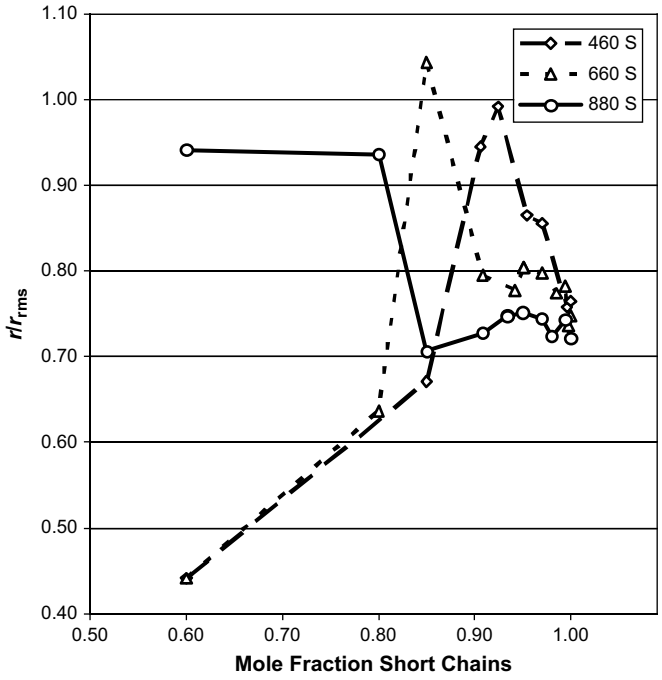

Fig. 6. Short chain connection RMS scaling factor, $\psi = r/r_{rms}$, for bimodal systems from Table 2 having short chain molecular weights of 460 (◇), 660 (△), and 880 (○) at the indicated short molar chain composition; $M_L = 21{,}300$ for each case. Lines drawn for clarity.

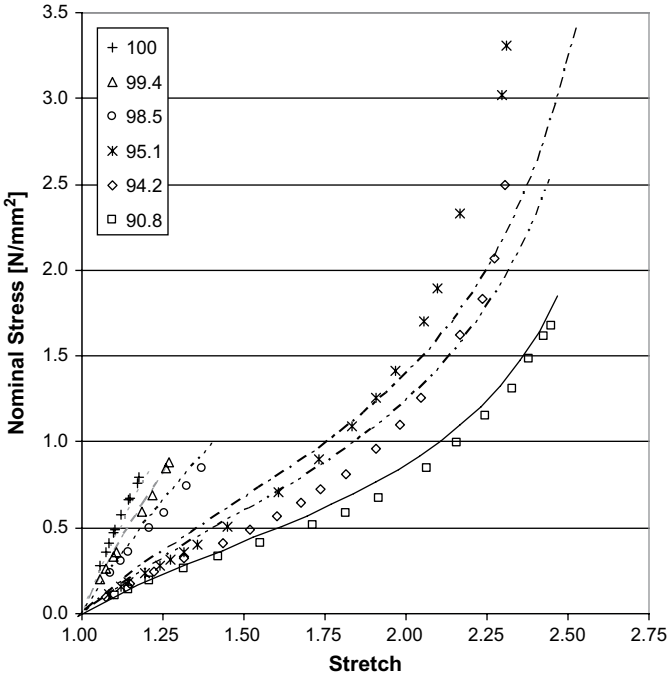

Fig. 8. Stress versus stretch ratio results of compression testing of bimodal PDMS, $M_L = 21{,}300$ and $M_S = 660$, with the mole fraction of short chains shown. Data are in symbols; best-fit bimodal chain theory without topology is given by lines. Data from Mark [1].

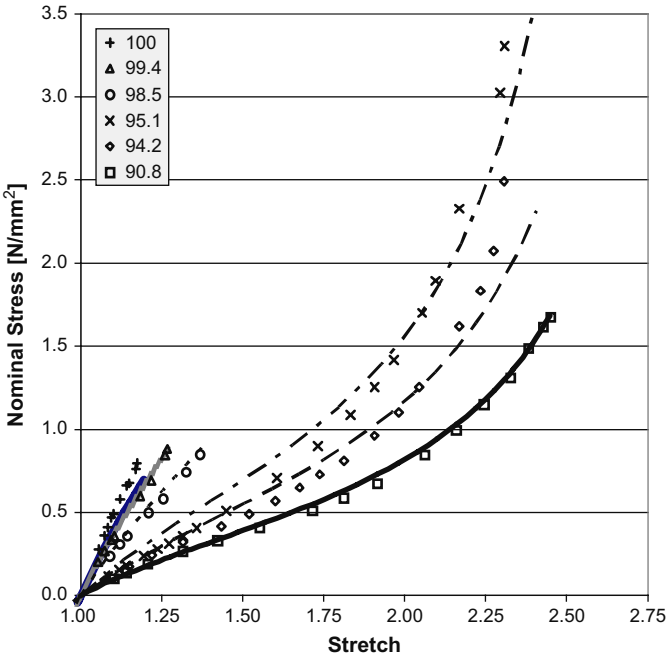

Fig. 9. Stress versus stretch ratio results of compression testing of bimodal PDMS, $M_L = 21{,}300$ and $M_S = 660$, with the mole fraction of short chains shown. Data are in symbols; best-fit bimodal chain theory with topology is given by lines. Data from Mark [1].

the average angle between a polarizing unit (which is, in its most irreducible form, a single monomer) and the draw axis [25]. Angled brackets denote averaging over all scattering units. Increased stretching and orientation of the polymer molecules are directly linked to the onset of locking and the resultant upturn in stress in uniaxial tension experiments [1–4,18,26]. At its extremes, the Herman's function has a value of 1 when the average polarizing unit is aligned with the draw axis and a value of $-1/2$ when it is perpendicular to the draw axis.

The notion that $\lambda_S \neq \lambda_L$ is itself straightforward and follows directly from equilibrium constraints, Eqs. (5)–(9). Several researchers have developed constitutive theories which predict this behavior as well [10,11]. These same constraints, however, namely Eq. (7), will yield equivalent birefringences, and thereby equal amounts of orientation as measured by the Herman's function, in Eqs. (27)–(30) if analyzed in a two-component (S, L) bimodal system since assuming force equilibrium will predict equivalent fractional extensions between the two components. The model derived here, however, provides a mechanism for differential stretching *and* orientation, also seen experimentally, in bimodal elastomer networks. This model's ability to characterize both stems from the inclusion of the S2 component. In spectral orientation measurements (such as IR dichroisim and Raman scattering) and calculations the S2 component is indistinguishable from the S since they both have the same chemical backbone and average molecular weight. Therefore, the S2 contributes to the orientation of the entire short chain fraction of the system, S + S2, based on its relative population in the system.

Fig. 10 shows a plot of the short chain orientation function versus molar short chain content for system 660 at a macroscopic stretch ratio of $\lambda = 1.2$ with and without the effects of topology in the constitutive model. The line without topology shows a slight

Table 3
Model parameters with no simulated topology information included

$\overline{n}_S$ = 2.9E20	N_S = 3.10	ψ_S = 1.0	ξ = 0.0
$\overline{n}_L$ = 1.0E17	N_L = 20.0	ψ_L = 1.0	

Table 4
Model fixed parameters with simulated topology information included

$\overline{n}_S$ = 2.6E20	N_S = 2.00
$\overline{n}_L$ = 7.0E18	N_L = 10.0

increase in short chain orientation as the molar short chain content is increased; the effect saturates between 70% and 91%, remaining relatively constant for $m_S \geq 91\%$. It is important to remember that the mechanical properties of system 660 were shown to change dramatically through the 90–100% short chain contents. Fig. 9 clearly shows a much larger increase in the short chain orientation function with increasing short chain content when topology is included. The figure also shows that through the $m_S = 90$–100% range the orientation function increases by nearly 50%.

Fig. 11 plots the combined short (S + S2), doubly connected short (S2), singly-connected short (S), and long (L) chain component orientation functions versus molar short chain content, m_S, for the same bimodal PDMS system with $M_S = 660$ and $M_L = 21{,}300$ at a macroscopic stretch ratio of $\lambda = 1.2$ with varying topology included. Force equilibrium leads to Eq. (9) which ensures that the L and S components have the same fractional extensions which, in turn, predicts equivalent orientations as seen in the figure. The graph also shows that the constitutive model predicts that the long chains (L) will slightly orient more than the combined short chains (S + S2) for the given amount of macroscopic stretch ratio;. This results from the low levels of orientation in the S2 component reducing the average orientation of the entire population of short chains, S + S2.

In Fig. 11 the model predicts Monnerie et al.'s finding that long chains orient more than the short chains in a bimodal system for a given amount of macroscopic stretch ratio. This prediction is also in line with Monnerie's finding that short chains orient less and long chains orient more in bimodal systems than their unimodal counterparts for a given amount of macroscopic stretch ratio. The short chain orientation (S + S2) drops off as more long chains are added and the long chain orientation (L) increases as more short chains are added. Below $m_S = 60\%$ the short and long orientations are nearly equivalent due to the vanishing populations of doubled connections. The low levels of orientation of the S2 component, wherever present in the figure, also shows the reinforcing, nature

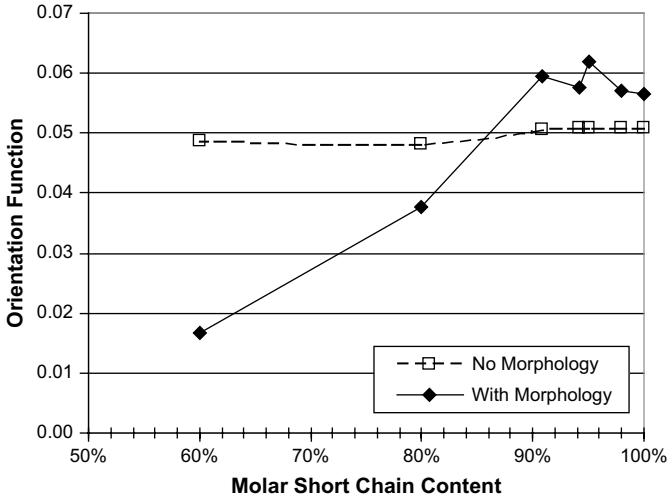

Fig. 10. Orientation function of entire network versus mole fraction short chains as predicted by bimodal theory with topology (solid line with diamonds) and without topology (dashed line with squares) for bimodal PDMS with $M_L = 21{,}300$ and $M_S = 660$. Values taken at a macroscopic uniaxial stretch ratio value of $\lambda = 1.2$.

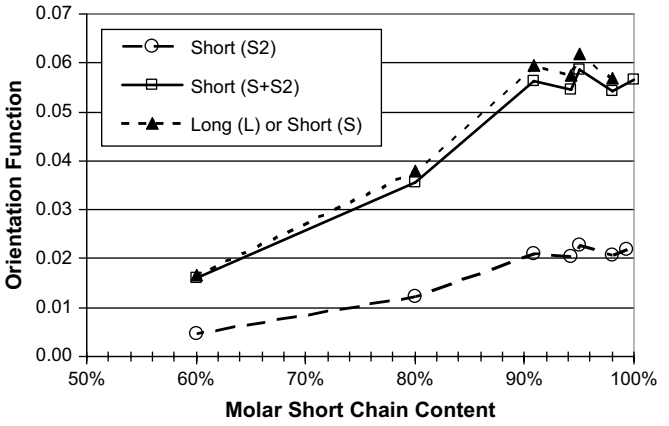

Fig. 11. Orientation functions of various bimodal chain components versus mole fraction short chains as predicted by bimodal theory with topology. S2 component has reduced orientation compared to S and L. Experimentally measured short chain response would follow S + S2 which is brought below L component due to S2 behavior thereby differentiating short chain and long chain behaviors in the bimodal system. Topological parameters are taken from simulations which model bimodal PDMS with $M_L = 21{,}300$ and $M_S = 660$; parameters for bimodal theory taken from best fit to data. Orientation values are calculated at a macroscopic uniaxial stretch ratio value of $\lambda = 1.2$.

of the doubly connected short chains which contract forcing compliance from the network.

5. Conclusions

The original bimodal chain model was extended to include computationally determined, composition-dependent changes in network topology. The inclusion of the computationally predicted S2, doubled connection, component into the original model's framework provides a micromechanics-based feature that shifts predicted stretch ratio–stress and stress–optic behaviors. The new model predicts load sharing in which the stiff S2 component forces compliance from both the less stiff long (L) *and* the singly-connected (and therefore less stiff) short (S) portions of the network. Load sharing is determined from the Herman's orientation function which measures both chain stretch ratio and orientation.

Without the inclusion of the S2 component, the original model, though able to predict differential stretching, predicted equivalent S and L component orientations in disagreement with published experimental results. The S2 component provides a load sharing mechanism that suggests explanations for differential orientations seen experimentally in bimodal networks and that captures trends across compositions. Specifically, the model predicts that the presence of the stiff, contractile, doubled connections forces the rest of the network to conform more to the macroscopic stretch ratio while reducing the measured average orientation of all short chains in the system; the effect diminishes as the composition-dependent population of doubled connections in the system decreases.

References

[1] Mark JE, Tang MY. Journal of Polymer Science: Polymer Physics Edition 1984;22:1849–55.
[2] Smith TL, Haidar B, Hedrick L. Rubber Chemistry and Technology 1990;63:256–64.
[3] Galiatsatos V, Mark JE. In: Zeigler JM, Fearon FWG, editors. Silicon based polymer science: a comprehensive resource. Washington, D.C: American Chemical Society; 1990. p. 201–6.
[4] Galiatsatos V, Mark JE. Macromolecules 1987;20(10):2631–2.
[5] Galiatsatos V, Subramanian PR. Makromolecular Chemistry, Macromolecular Symposium 1993;76:233–40.
[6] Soni VK, Stein RS. Macromolecules 1990;23:5257.
[7] Oikawa H. Polymer 1992;33:1116.
[8] Monnerie L, Besbes S, Cermelli I, Bokobza L, Bahar I, Erman B, et al. Macromolecules 1995;28:231–5.
[9] Bahar I, Erman B, Bokobza L, Monnerie L. Macromolecules 1995;28:225–31.
[10] Mark JE, Curro JG. Journal of Chemical Physics 1983;79:5705–9.
[11] Llorente MA, Rubio AM, Freire JJ. Macromolecules 1984;17:2307–15.
[12] von Lockette PR, Arruda EM. Macromolecules 2002;35:7100–9.
[13] Termonia Y. Macromolecules 1990;23:1481–3.
[14] Madkour T, Mark JE. Macromolecular Reports 1994;31(1–2):153–60.
[15] Hagn C, Wittkop M, Kreitmeier S, Trautenberg HL, Holzl T, Goritz D. Polymer Gels and Networks 1997;5:327–37.
[16] von Lockette PR, Arruda EM. Macromolecules 1999;32:1990–9.
[17] von Lockette PR, Arruda EM. Computational and Theoretical Polymer Science 2001;11:415–28.
[18] Treloar LRG. The physics of rubber elasticity. Oxford, UK: University Press; 1975.
[19] Arruda EM, Boyce MC. Journal of the Mechanics and Physics of Solids 1993;41(2):389–412.
[20] von Lockette PR, Arruda EM. Acta Mechanica 1999;134:81–107.
[21] Arruda EM, Przybylo PA. Polymer Engineering 1995;35(5):395–402.
[22] Nagai K. The Journal of Chemical Physics 1963;40(10):2818–26.
[23] Eicheinger BE, Leung YK. Journal of Chemical Physics 1984;80:3877–84.
[24] Eichinger BE, Leung YK. Journal of Chemical Physics 1984;80:3885–91.
[25] Gedde UW. Polymer physics. New York: Chapman and Hall; 1995.
[26] Mark JE. Advances in Polymer Science 1982;44:1–25.